CHAPTER V
MECHANICAL, RHEOLOGICAL, AND SWELLING BEHAVIORS OF NATURAL RUBBER/MONTMORILLONITE AEROGEL COMPOSITES PRODUCED BY FREEZE-DRYING

5.1 Abstract

Montmorillonite (Na^+-MMT) aerogel/prevulcanized natural rubber (PNR) latex composites were produced using the environmentally friendly/benign process known as freezing-drying. The composites exhibited densities in the range of 0.36–0.51 gcm^{-3}, which is in good agreement with the content of polymer in the aqueous solutions. The level of dispersion of the Na^+-MMT and the microstructure of the composites were characterized by means of X-ray diffraction analysis and scanning electron microcopy, respectively. The influence of Na^+-MMT particles on the mechanical, rheological and swelling properties of the resulting composites were investigated as well. The results reveal that a composite made from 7 parts per hundred of rubber (phr) loading of Na^+-MMT showed the greatest improvement in material properties, as can be observed from the mechanical and melt rheological tests data. It is anticipated that such Na^+-MMT aerogel/polymer composites will be excellent candidates for utilizing in a range of structural and insulation applications.

Keywords: Aerogels; Nanocomposites; Mechanical properties; Analytical modeling; Rheology

5.2 Introduction

A great deal of attention has been devoted over the past decade to the development of lightweight and high performance materials which meet the needs of transportation, aerospace, and consumer applications. This reduction in materials weight has been accomplished by utilizing the composite materials, in which the organic and inorganic components act synergistically to yield the required properties without sacrificing the physical properties of the organic matrix [Lee et al., 2009]. Nanocomposites comprised of highly anisotropic layered silicates (aspect ratio of 1000 or greater) often provide the exceptional performance in terms of mechanical strength, heat resistance, barrier resistance against gases (e.g. oxygen, nitrogen and carbon dioxide), water and hydrocarbons, and UV stability, as compared to individual organic polymers or conventional filled composites [Teh et al., 2004 and Raka et al., 2009]. These improvements are usually achieved with small quantities of the clay particles (less than 10 wt%) in order to ensure a good dispersion of the silicate layers in the polymer matrix and an optimized interaction at the interface between two phases [Raka et al., 2009].

From the development of nanoscience and nanotechnology viewpoint, the most extensively used layered silicate is natural sodium montmorillonite (Na^+-MMT) which is a well-known source of reinforcement for polymers. Owing to its ability to form gel in water, these smectite can be converted into 'house of cards'-like aerogels with bulk densities typically in the range of 0.01-0.1 gcm^{-3} (void volume fraction ~ 95 %) through a robust and environmentally-benign freeze-drying process [Bandi et al., 2005; Bandi et al., 2006; Somlai et al., 2006; Arndt et al., 2007; Finlay et al., 2008; Gawryla et al., 2008; Gawryla et al., 2009a; Johnson III et al., 2009]. During the freezing of aqueous clay dispersions, the growing ice fronts cause alignment/shearing of the Na^+-MMT platelets along the ice crystal faces to produce lamellar structures, which, after high vacuum sublimation, result in ultra low density layered superstructures. As the neat aerogels are relatively fragile and possess poor mechanical strengths, the incorporation of either a polymeric component and/or natural or synthetic fibers into the framework of Na^+-MMT aerogel is required for improving its mechanical rigidity and for producing the foam-like structures that

reflect the thermal/mechanical properties of the matrix polymers themselves. A wide range of organic polymers such as poly (*N*-isopropyl acrylamide) [Bandi et al., 2005], poly(vinyl alcohol) [Bandi et al., 2006 and Finlay et al., 2008], epoxy precursors [Arndt et al., 2007], casein [Gawryla et al., 2008], poly (ethylene imine) [Johnson III et al., 2009] have been incorporated into the aqueous aerogel precursor dispersion prior to freeze-drying, and the results showed a successful improvement in the mechanical properties of the aerogels while retaining the polymer/aerogel composites made with density in the range of 0.05 to 0.15 gcm^{-3}. Similar reinforcement was found after incorporating the natural or synthetic fibers into the aqueous aerogel precursors as well [Finlay et al., 2008 and Gawryla et al., 2009a]. The resulting polymer/aerogel composites are the promising materials for many applications, including thermal and acoustic insulation, low-pressure-drop catalysis, and structural materials in transportation [Gawryla et al., 2009a].

Although the latex compounding method was utilized before in producing the natural rubber (NR)-based nanocomposites [Varghese et al., 2003 and Stephen et al., 2006], there are no reports of polymer/Na^+-MMT aerogel composites, utilizing prevulcanized natural rubber (PNR) latex as the organic polymer, prepared by the above-mentioned freeze-drying to date. In the present study, a single freezing-drying step was applied for producing the Na^+-MMT aerogel/PNR latex composites from the aqueous PNR latex/Na^+-MMT gels. The structure of the composites was investigated by X-ray diffraction and scanning electron microscopy. The compressive, dynamic thermo-mechanical, and transport properties were examined as a function of Na^+-MMT loading. Lastly, the rheological behavior was studied in order to understand the structure–property relationship of the resulting materials.

5.3 Experimental Parts

5.3.1 Raw Materials

Pristine Na^+-MMT (Kunimine Industries Co., Ltd., Kunipia grade), with a cation exchange capacity (CEC) of 115 meq/100g, and centrifuged NR latex with 60% dry rubber content were used without further modification. The compounding ingredients i.e. potassium hydroxide, zinc oxide, calcium carbonate,

zinc diethyl dithiocarbamate (ZDEC), wingstay-L, and sulfur were purchased from the Rubber Research Center, Kasetsart University (Thailand) and used as received.

5.3.2 Preparation of the Composites

As received 60wt% NR latex was first diluted to 30wt% latex with distilled water, and was further used as a raw material for preparing the prevulcanized latex according to the formulations given in Table 5.1. The prevulcanization of the compounded latex was conducted at 70°C for 30 min under the high speed stirring (7000 rpm). In a second 2 liter container, 20 g of Na^+-MMT was blended with 1000 g distilled water under vigorous stirring for 2 h in order to wet out the Na^+-MMT, and then the mixture was mixed at high speed for 30 min using a homogenizer to create a 2wt% Na^+-MMT dispersion. Afterwards, the designated amount of Na^+-MMT dispersion was slowly added into the prevulcanized latex under vigorous stirring for 2 h, followed by homogenizing stirring for another 30 min at room temperature.

Aqueous solutions obtained in this manner were poured into 2.5 cm diameter cylindrical glass vials for making cylindrical test specimens and were subsequently frozen in a –80°C freezer. The frozen samples were then transferred to a Scanvac freeze-dryer with a condenser temperature of -108°C and subjected to very high vacuum (< 0.1 mbar) in order to sublime the ice. After 3 days in the freeze-dryer, the samples were removed and then cured in an oven at 150°C for 30 min. Control samples were made according to the above-mentioned procedure without the incorporation of Na^+-MMT. In the sample coding, PNR stands for the prevulcanized rubber latex, M represents the Na^+-MMT, and the numbers 1, 3, 5 and 7 indicate the mass content of Na^+-MMT used.

5.3.3 Characterizations

X-ray diffraction patterns were recorded in the range of 2θ = 1–40° (interval of 0.02°) on a Bruker AXS Model D8 Discover X-ray diffractometer, with Ni-filtered Cu Kα (λ = 0.154 nm) radiation operated at 40 kV and 40 mA. The basal spacing (d_{001}-spacing) was calculated according to the Bragg equation ($\lambda = 2d\sin\theta$).

The morphological features of the composites were investigated using a JEOL, Model JSM5200 scanning electron microscope. The samples were fractured in a liquid nitrogen bath, placed on a sample holder using carbon adhesive tape, and then sputter-coated with gold under vacuum to prevent the electrostatic charging during observation.

The cure characteristics of the composites were determined at four different temperatures ranging from 150 to 180°C using a torque rheometer (ODR). The kinetic parameters viz. specific rate constant (K) and apparent activation energy (E_a) were calculated from the torque–time curves according to literature equations [Kader and Nah, 2004 and Chandran and Narayanankutty, 2008].

A gravimetric procedure was adopted to monitor the swelling behavior of the composites. The thickness and initial weight of the samples were taken prior to the swelling experiment. Samples were then immersed in 80 ml toluene at 25°C and filtered out at regular intervals of time using a mesh sieve. The swollen samples were then drained on the sieve to remove the adhering solvent, and weighed immediately on the electronic balance. Such procedure was continued until the equilibrium swelling was attained for each sample. The solvent adsorption (Q_t) and the swelling kinetics were determined on the basis of the mass changes [Stephen et al., 2006 and Siddaramaiah et al., 2008]. The crosslink density (V_e) and thermodynamic parameters were also computed using the Flory–Rehner and Flory–Huggins equations, respectively [López-Manchado et al., 2003 and Pojanavaraphan and Magaraphan, 2008].

Compression testing was carried out using a Universal Testing Machine (LLOYD LR 100K) at a constant strain rate of 10 mm/min according to ASTM D575-91. Five samples of each composition were tested, and the compressive moduli were calculated from the slopes of the linear portions of the stress–strain curves.

Dynamic mechanical analyses were conducted on a TA Instruments Q800 DMA machine fitted with a tensile testing head in the temperature ranging from -80°C to +130°C at a rate of 3°C/min. A static force of 10 mN was applied to ensure that the samples were taut between the tensile grips, and the rectangular

samples were scanned using the fixed frequency of 10 Hz and the amplitude of 25 μm.

Rheological measurements were carried out on a Rubber Process Analyzer (RPA 2000, Alpha Technologies) under the oscillatory shear. All studies were conducted at the temperature of 150°C. Dynamic strain sweep tests were initially performed for strains between 0.28 and 140% at a constant frequency of 0.63 rad/s in order to assess the limits of the linear viscoelastic regime. Dynamic frequency sweeps were performed over the frequency range of 0.1-100 rad/s at the constant strain amplitude of 5%.

5.4 Results and Discussion

5.4.1 X-Ray Diffraction and Scanning Electron Microscopy Analyses

The extent of intercalation of polymer chains into the interlayer space can be determined from the XRD patterns in the range of 2θ = 1-10°. The XRD patterns of the neat Na^+-MMT and the corresponding composites are given in Figure 5.1. Na^+-MMT powder displayed the well-defined d_{001} reflection at 2θ = 7°, which corresponds to a mean basal spacing of 1.25 nm. In the case of PNR composites, the intensity of the characteristic peak of Na^+-MMT was reduced owing to the dilution effect, and there was a shift in the angle of reflection towards the lower position, which corresponds to the basal spacing of 4.30, 4.19, 4.76, and 4.88 nm for PNR/M1, PNR/M3, PNR/M5, and PNR/M7, respectively. This increase in basal spacing was a strong indication that the structure of the composites made was highly intercalated, and such dispersion technique can be considered as an efficient method for providing a good dispersion of the silicate layers having a strong polarity into the rubber matrix. Meanwhile, the peaks at 2θ = 31.6° and 36.1° were assigned as the (100) and (101) reflections, respectively, of ZnO particles [Guo et al., 2009] present within the composites. As noted, despite a great change in the bulk density from 2.83 to 0.05 gcm^{-3}, the basal spacing of the Na^+-MMT aerogel (not shown here) remained almost the same as that of the starting Na^+-MMT [Gawryla et al., 2009a].

SEM micrographs of Na^+-MMT aerogel and the corresponding composites are depicted in Figure 5.2. The Na^+-MMT aerogel (Figure 5.2a) exhibited

a characteristic lamellar structure (a series of parallel Na^+-MMT sheets) which was a replica of the ice crystal morphology [Gawryla et al., 2009a]. In case of composite with 1 phr Na^+-MMT (Figure 5.2c), it appeared that the concentration of Na^+-MMT in the starting aqueous gel was not enough (less than 0.7 wt%) for producing a highly lamellar morphology [Somlai et al., 2006], whereas in the case of composites with 5 and 7 phr Na^+-MMT, a regular layered superstructure was produced and completely covered/connected by the layer of NR matrix, as shown in Figure 5.2d and e, respectively. That the concentration of Na^+-MMT in the aqueous precursor dispersion plays a key role for producing such three dimensional (3D) Na^+-MMT networks was consistent with earlier discussions which concluded that hydrogelation of the Na^+-MMT at or above its 2 wt% gel point was necessary in order to achieve a persistent aerogel structure upon freeze-drying [Somlai et al., 2006]. Based on the SEM micrographs, the schematic model describing the structure of composites made was proposed and is depicted in Figure 5.3.

5.4.2 Cure Characteristics and Kinetics

There are many parameters which have an influence on the vulcanization properties of the elastomeric-based materials; this study focused on the effect of temperature and Na^+-MMT loading. The rheographic profile of PNR and its composites obtained at 150°C is shown in Figure 5.4, and their cure characteristics are listed in Table 5.2. Irrespective of the cure temperature, the addition of the Na^+-MMT increased the maximum torque (D_{max}) noticeably especially at 5 and 7 phr loading, while providing a trivial difference in the optimum cure time (t_{90}) compared to that of the neat PNR. This was probably due to the faster cure in the early stage of reaction than the latter stage [Kader et al., 2006]. The higher value of D_{max} for the composites indicated the reinforcing nature of the Na^+-MMT particles and the formation of confined elastomeric network within the interlayer space [Kader and Nah, 2004]. However, a slight decrease in D_{max} upon addition of 1 phr Na^+-MMT pointed to the cure retardation effect of Na^+-MMT by adsorbing part of curative on top of its surface, which would reduce the amount of curatives available for the cure reaction [Kader and Nah, 2004]. Similar conclusions can be reached with the kinetic parameters and the swelling studies, which will be discussed shortly.

The kinetic parameters e.g. specific rate constant (K) and activation energy (E_a) were determined from the rheometric data by utilizing the equations given below:

$$\ln(D_{max} - D_t) = -kt + \ln(D_{max} - D_{min}) \quad (5.1)$$

$$K(T) = K_0 \exp(-E_a / RT) \quad (5.2)$$

where D_t and D_{min} are the torque values at a given time and time zero, respectively, k or $K(T)$ is the first-order rate constant at a temperature T, and R is the universal gas constant. If a plot of ln (D_{max}-D_t) against time (t) yields a straight line, then the cure reaction follows the first-order kinetics, and the first-order rate constant can be calculated from the slope of the corresponding straight line. The activation energy of the curing process was determined using the Arrhenius equation (Eq. (5.2)), and the values are listed in Table 5.2 along with the specific rate constant.

As expected, the plot of ln (D_{max}-D_t) against time for PNR and its composites at 150°C was found to be linear (Figure 5.5a), which supports the suitability of the first order kinetic model for analyzing the cure behavior in the present system. As the kinetic rate constant was derived from the torque, the addition of Na^+-MMT resulted in an increase in the k values. Similar to the effect of Na^+-MMT, the temperature had an influence on the vulcanization process. Increasing the cure temperature increased the k values and decreased the t_{90} of the composites [Kader and Nah 2004]. This was due to the availability of more thermal energy for the cure reaction (acceleration effect). To understand more about the vulcanization kinetics, the value of E_a of curing reaction was computed from the Arrhenius plot of ln K versus $1/T$, as depicted in Figure 5.5b. The existence of Na^+-MMT increased the E_a value from 46.91 (without Na^+-MMT) to 76.83 (with 7 phr Na^+-MMT) $kJmol^{-1}$; in other words, a higher amount of energy was required for the curing of composites. This verified the cure retardation effect of Na^+-MMT by adsorbing part of the curing agents on its surface and blocking the movement of rubber chains.

5.4.3 Swelling Behavior and Transport Mechanism

A decrease in cross-linking efficiency was verified by the examination of the swelling behavior, the equilibrium swelling ratio (Q_f), and the number of

network chain segments per unit volume (V_e). A plot between the fraction of toluene uptake (Q_t) and time ($t^{1/2}$) of PNR and its composites is displayed in Figure 5.6a. Two different regions can be seen from these adsorption curves. The first region denotes the high swelling rate because of the large concentration gradient, and the samples are under severe solvent stress, whereas the second zone indicates a reduced swelling rate due to a decrease in concentration gradient, and the swelling process almost reaches the equilibrium [Stephen et al., 2006]. The initial swelling rate of composites increased rapidly and reached the equilibrium within small times, relative to the standard neat PNR. As a result, the equilibrium solvent uptake of the composites increased as a function of Na^+-MMT loading, and simultaneously the crosslink density decreased, as listed in Table 5.3. These swelling results were in accordance with the results obtained from the rheometer that the curing process was restricted upon the addition of Na^+-MMT, even though it was reported that the adsorption of solvent can be reduced in the nano-filled systems due to the enhanced polymer/filler interaction, the highly tortuous path and the reduced transport area [Stephen et al., 2006]. A similar trend was found in the case of PNIPAM/Na^+-MMT aerogel composites utilizing polyhedral oligomeric silsesquioxane (POSS) as a cross-linking agent [Bandi et al., 2005].

Another plausible reason for the rapid swelling rate of the composites was explained by the existence of voids, created after subjecting to a high vacuum freeze-drying. This would increase not only the availability of spaces for accommodating the solvent molecules but also the contact area between the polymeric layer, coating the majority of silicate surfaces, and the solvent, causing the polymer chains to swell. In other words, the segmental motion rate was now much greater than the rate of diffusion of permeant molecules, although some polymer chains were intercalated in the interlayer space of Na^+-MMT, as evidenced from the previous XRD patterns. This concept fitted well with the rapid water uptake for the lamellar materials, as discussed by Gawryla and Schiraldi [Gawryla and Schiraldi, 2009b].

By making the assumption that there was no change in the internal energy of the studied materials upon swelling, the thermodynamic aspects (Table 5.3) can be analyzed through the Flory–Huggins equation:

$$\Delta G = RT\left[\ln(1-\phi_r)+\phi_r+\chi\phi_r^{\,2}\right] \quad (5.3)$$

$$\Delta G = -T\Delta S \quad (5.4)$$

where ΔG and ΔS are the elastic Gibbs free energy and the conformational entropy, respectively, χ is the Flory–Huggins polymer–solvent interaction (0.391), and φ_r is the volume fraction of rubber. Since the studied materials exhibited the negative value of ΔG, this verified a good compatibility between the Na^+-MMT and rubber matrix. Besides, the decrease of conformational entropy indicated the formation of 3D Na^+-MMT networks, particularly at 7 phr loading.

As a plot of Q_t against $t^{1/2}$ gave a straight line at short time (shown as inlay in Figure 5.6a), the diffusion coefficient of toluene (D) can be computed from the initial slope using the following equation:

$$Q_t / Q_\infty = (4/h)(D/\pi)^{1/2}(t)^{1/2} \quad (5.5)$$

where h is the initial thickness of sample, and $Q_t/t^{1/2}$ is the slope of an initial portion of the sorption curve. The toluene diffusivity of the composites increased as a function of Na^+-MMT concentration (see Table 5.4), and this was mainly a result of a decrease in the crosslink density value upon Na^+-MMT addition. To understand more about the diffusion process, the transport properties of the studied materials were described using the empirical equation:

$$\log(Q_t / Q_\infty) = \log k + n \log t \quad (5.6)$$

where n (slope) and k (y-intercept) values indicate the transport mechanism and the nature of interaction between polymer and solvent, respectively. Three basic modes of transport can be distinguished [Stephen et al., 2006 and Siddaramaiah et al., 2008], which is Fickian for n = 1/2, non-Fickian for n = 1, and non-Fickian anomalous transport behavior for $1/2 < n < 1$. The plot of log (Q_t/Q_∞) versus log t is presented in Figure 5.6b, and the transport parameters are summarized in Table 5.4. The PNR itself exhibited the Fickian behavior with the k value equal to 2.9×10^{-2}. In the case of composites, the transport mechanism was no longer the Fickian behavior, and the k values were apparently higher relative to the standard neat PNR, mainly at 5 and 7 phr loadings. This was an indicative of the reduction in the amount of crosslink and the higher interaction between rubber matrix and solvent (the higher the k value, the stronger the interaction between rubber and solvent), giving rise to a

large segmental motion and separation between the rubber chains. In other words, the swelling process was no longer diffusion controlled and reached the equilibrium within short time. Such observation trend was corroborated by the equilibrium solvent uptake and the solvent diffusivity data mentioned above.

5.4.4 Compression Test

The compression curves of the studied materials are shown in Figure 5.7. Polymeric foams often undergo the linear–elastic response at an initial loading, followed by the horizontal plateau upon increasing the compression load, and finally reach the densification region where the voids are entirely collapsed [Wouterson et al., 2005; Gawryla et al., 2008; Johnson III et al., 2009]. The initial modulus is always utilized, as it is an indication of the genuine material response before experiencing the permanent damage. As would be expected, the addition of Na^+-MMT led to a monotonic increase in the compressive modulus of the resulting materials (see Table 5.5). This was explained by the good interfacial adhesion between the matrix and clay mineral layer, being capable of dissipating the input energy. To elucidate the dependence of the mechanical behaviors of composites on the Na^+-MMT content, the reinforcing efficiency [Kim et al., 2009] was computed from the initial modulus and is presented in Table 5.5. The PNR/M7 composite possessed the greatest reinforcing efficiency of Na^+-MMT (~ 81%) compared to the others, and this signified that the 3D layered structure played a dominant role in creating the more effective energy-dissipation mechanism under the applied stress.

According to the literature [Arndt et al., 2007; Finlay et al., 2008; Gawryla et al., 2008; Johnson III et al., 2009; Gawryla et al., 2009a], the neat Na^+-MMT aerogel produced from 5 wt% solution in water had the initial modulus of 10 kPa, but once combining with the polymeric binders, more rigid and foam-like structures were produced with the compressive modulus ranging from several hundred to thousand kPa, depending on the molar mass and concentration of the organic polymers used. In the present study, while the addition of Na^+-MMT reinforced the composites, their compressive moduli were much lower than those of previous reports. Incomplete vulcanization of the materials would explain the relatively low mechanical properties of the NR composite materials (see Table 5.5).

The aerogel materials would exhibit superior thermal insulation characteristics compared to those of dense polymers [Arndt et al., 2007 and Gawryla et al., 2008].

5.4.5 Dynamic Mechanical Test

DMA is often utilized for studying the viscoelastic characteristics and relaxation processes in polymers and polymer composites [Kader et al., 2006]. Results of the DMA measurements are collected in Figure 5.8a and b, where the dynamic storage modulus (E') and loss tan δ factor of the neat PNR and its composites are plotted against the temperature, respectively. The storage modulus of the composite with 1 and 3 phr Na^+-MMT loadings did not change drastically compared to that of the neat PNR, whereas at the 5 and 7 phr Na^+-MMT loadings, a complicated scenario was observed, depending on whether the temperature was below or above the glass transition temperature (T_g). In the glassy state (below T_g), the storage moduli of the composites decreased with increasing the Na^+-MMT content, particularly at 5 phr loading. This decrease was opposite to the well-known reinforcing nature of the Na^+-MMT for the dense composites either in the glassy state or rubbery region. Such finding was an indicative of the void effect, which caused the initiation of catastrophic failure upon subjecting to the dynamic cyclic loading [Gatos et al., 2004 and Wouterson et al., 2005], followed by a deterioration in their elastic properties. In the rubbery regime (above T_g), on the other hand, the 3D Na^+-MMT networks as well as interfacial bonding between the rubber matrix and Na^+-MMT played the leading role in controlling the mechanical response of the aerogel materials. As a result, despite the presence of voids, there was a significant increase in material's stiffness, mainly at 7 phr loading, where the 3D networks were formed. This verified the great contribution of the lamellar structure in reinforcing the aerogel composites above T_g. Our results happened in the similar manner as those of Yoo and Paul [Yoo and Paul, 2008] in that the reinforcing effect of Na^+-MMT became greater, as the modulus of amorphous polyamide decreased in going from the glassy state to rubbery state.

The loss tangent curves (see Figure 5.8b) are widely used for determining the molecular mobility and the glass transition temperature of the materials. The tan δ peak value of the composites decreased monotonically with

increasing the Na^+-MMT content, confirming the decrease in macromolecule's mobility near the interface, particular at 7 phr loading [Gatos et al., 2004; Kader et al., 2006; Pojanavaraphan and Magaraphan, 2009; Samakande et al., 2009]. No significant change in the T_g value of the composites was observed in comparison with that of pure PNR matrix, which was about –50°C. Similar trend was found in our previous work [Pojanavaraphan and Magaraphan, 2009].

A comparative study of the experimental data with the values predicted from the composite theories was made in order to characterize the reinforcing efficiency of the Na^+-MMT. Herein, Guth [Guth, 1945] and Halpin–Tsai [Halpin, 1969 and Halpin and Kardos, 1976] equations were chosen, and the modeling was done on the dynamic modulus values at room temperature (25°C). As the contribution of platelet-like silicate layers to the modulus of composites is expected to be less than fiber-like filler at the same volume fraction, the modulus reduction factor (MRF) is introduced into the Guth's equation [Wu et al., 2004 and Gatos et al., 2007]. This is given as follows:

$$E = E_m\left[1 + 0.67(MRF)\alpha\phi + 1.62(MRF)^2(\alpha\phi)^2\right] \qquad (5.7)$$

where E and E_m are the modulus of composite and rubber matrix, respectively, α is the shape factor (i.e. width/thickness), the value of MRF is ~0.66, and φ is the volume fraction of Na^+-MMT. Similarly, to improve the predictive ability of the Halpin–Tsai equation, the MRF is introduced, and the Halpin–Tsai equation is then transformed into the following equation [Wu et al., 2004]:

$$E / E_m = \left[1 + (MRF)(\xi\eta\phi)\right]/\left[1 - \eta\phi\right] \qquad (5.8)$$

$$\eta = \left(E_f / E_m - 1\right)/\left(E_f / E_m + \xi\right) \qquad (5.9)$$

where ξ is a shape parameter, E_f is the Young's modulus of Na^+-MMT platelets (~170 GPa), and η is a parameter whose magnitude depends on the type of filler. For perfectly oriented lamellar shape filler reinforcements such as rectangular Na^+-MMT platelet, ξ is equal to 2α, and the value of η is close to 1 owing to the much greater contribution of Na^+-MMT platelet tension modulus compared to the neat matrix [Wu et al., 2004 and Praveen et al., 2009]. Note that the aspect ratio of the silicate layers was assumed to be ~100, and the densities of 2.83 [Fornes and Paul, 2003] and 0.49

gcm^{-3} were taken for the Na^+-MMT particles and the neat rubber matrix, respectively.

As depicted in Figure 5.9, the experimental storage modulus of the composites increased with the Na^+-MMT volume fraction, as expected, and showed a positive deviation from the theoretically predicted values. In fact, the positive deviation became more significant in case of a sample containing 7 phr of Na^+-MMT, and this suggested that the models were quite suitable for the dense composites bearing either highly exfoliated or highly aggregated structures [Wu et al., 2004; Gatos et al., 2007; Praveen et al., 2009]; but not did for the aerogel materials possessing the lamellar morphology. Since the layered superstructure had the ability to absorb and transfer the applied load on the basis of a layered system [Johnson III et al., 2009], it was not surprising why the 3D structure was more effective in reinforcing the mechanical strength of the aerogel composites, particularly above their glass transition, which is known as the working temperature of the rubber materials. This feature was identical to the reinforcing mechanism in these lamellar materials upon exposure to the compressive loading, as described above.

5.4.6 Rheological Behavior

Characteristic rheological properties of polymer nanocomposites were measured in order to achieve a fundamental understanding of the processability and structure–property relationship of these materials. According to Manitiu et al. [Manitiu et al., 2009], the viscoelastic response depends primarily on the following parameters: the volume fraction of Na^+-MMT, its dispersion state, and the extent of interactions between polymer and Na^+-MMT including between Na^+-MMT itself. As the studied materials possessed the same dispersion state of Na^+-MMT and similar level of polymer–filler interactions, we suggested that the volume fraction of Na^+-MMT and the interaction between Na^+-MMT itself played a dominant role for the rheological differences between these samples.

The strain dependence of storage modulus (G') at 150°C obtained by strain sweep tests for the PNR matrix and the composites, having 1 and 7 phr Na^+-MMT loadings, is shown in Figure 5.10. Herein, the contribution of void fraction to

material properties was negligible, as the samples were loaded and compressed within a torsional dynamic rheometer. The results for the neat PNR and PNR/M1 composite were very similar; that is, there was no significant variation in G' value with increasing the double strain amplitude up to 20%. This plateau, which is often seen either with the gum rubber or low filled materials [Leblanc, 2002], corresponded to the linear viscoelastic region of the studied materials. Therefore, 5% strain was utilized for conducting the dynamic frequency sweep analyses, which will be discussed shortly. In the case of PNR/M7 composite, the storage modulus was much greater than that of the PNR and PNR/M1 samples, and a strong dependence of G' on the double strain amplitude was evidenced. This phenomenon was known as the 'Payne effect', in which the 3D percolating networks formed by the edge-to-face interactions of the Na^+-MMT platelets were destroyed at higher shear amplitude, causing a decrease in the value of G' [Wagener and Reisinger, 2003; Das et al., 2008; Manitiu et al., 2009]. It was well documented that the theoretical value of inorganic matter required for percolation to occur was in the range of 4–7 wt%, depending on the type and density of clay used [Manitiu et al., 2009]. Compared to our study, since the weight fraction of Na^+-MMT particles in PNR/M7 composite was ~ 6 wt%, it was concluded that the Na^+-MMT platelets had rearranged themselves into the percolated networks (so-called 'house of cards' structure), which contributed to the significant enhancement in G' of the composite, particularly at low shear amplitude.

The frequency dependence of complex viscosity (η^*) at 150°C for the neat PNR and its composites is depicted in Figure 5.11a. The studied materials displayed the same pattern of complex viscosity curves; that is, η^* decreased linearly with an increase in the angular frequency, and their shear thinning exponent (n) values were very close to –1. This was an indicative of the typical non-Newtonian behavior (solid-like response), as reported in literature [Samakande et al., 2009]. Furthermore, the PNR/M7 composite showed an approximately 500% improvement in η^* at low frequencies relative to the neat PNR, and this emphasized an impact of the inorganic matter on the segmental relaxation dynamics of polymer chains. The variation of storage modulus (G') and loss modulus (G'') with angular frequency for the neat PNR and its composites is presented in Figure 5.11b. The composites as well as the neat PNR itself exhibited frequency independent dynamic moduli with $G' > G''$

over the whole frequency range measured. A non-terminal solid-like behavior, in accordance with the complex viscosity results, was therefore indicated here. Note that in the case of monodisperse unfilled polymers, the G' and G'' moduli exhibit the classical ω^2 and ω^1 dependence on angular frequency in the terminal flow regime; therefore, any deviations from these values point to the influence of polydispersity index and the existence of Na^+-MMT particles [Wagener and Reisinger, 2003; Manitiu et al., 2009; Samakande et al., 2009]. In addition, the composite containing 7 phr Na^+-MMT had the greatest improvement both in the G' and G'' moduli relative to the neat matrix, and this was a result of the reinforcing effect of Na^+-MMT as well as the formation of strongly interacting Na^+-MMT networks [Wagener and Reisinger, 2003; Manitiu et al., 2009; Samakande et al., 2009].

5.5 Conclusions

In this study, an environmentally benign process was applied for preparing the clay aerogel/PNR latex composites. The addition of Na^+-MMT reduced the availability of curatives (cure retardation effect) and increased the activation energy for the curing reaction, as computed from the first-order kinetics model. The viscoelastic response of the composites was influenced by not only the volume fraction of Na^+-MMT but also the extent of interaction between Na^+-MMT itself. A detailed study of the transport properties revealed a deviation from the Fickian behavior upon the incorporation of Na^+-MMT; that is, the diffusion process was no longer dependent on the chemical potential since the lamellar materials adsorbed the solvent almost instantaneously through the capillary action. Unlike the dense composites in which the mechanical robustness primarily depended on the filler volume fraction and the extent of interfacial bonding, herein, careful attention must be paid to the void volume fraction as well as the crosslink density, being the additional key factors that control the mechanical behavior of the aerogel materials. Although, the great reinforcing efficiency of the 3D Na^+-MMT networks to the materials' properties was evidenced above the glass transition, based on DMA and compression tests, a longer cure time was necessitated to optimize the mechanical integrity of the aerogels, when compared with the others reported up to date. In short,

despite the existence of voids, the layered superstructure was better at reinforcing the composites above T_g and ultimately offered the rapid solvent adsorption capability, which would enable the possibility of using these as structural, insulation, and/or highly adsorbent materials in many applications, wherein low density is of great importance.

5.6 Acknowledgements

The authors are grateful to the Thailand Research Fund through the Royal Golden Jubilee Ph.D. Program (PHD/0088/2549), the Rachadapisek Sompoch Endowment, and Center for Petroleum, Petrochemicals, and Advanced Materials, Chulalongkorn University, for providing financial support. We would also like to acknowledge Prof. Alexander M. Jamieson for insightful discussions on rheological phenomena.

5.7 References

Arndt, E.M., Gawryla, M.D., Schiraldi, D.A., 2007. Elastic, low density epoxy/clay aerogel composites. J Mater Chem 17, 3525-3529.

Bandi, S., Bell, M., Schiraldi, D.A., 2005. Temperature-responsive clay aerogel–polymer composites. Macromolecules 38, 9216-9220.

Bandi, S., Schiraldi, D.A., 2006. Glass transition behavior of clay aerogel/poly(vinyl alcohol) composites. Macromolecules 39, 6537-6545.

Chandran, A.S., Narayanankutty, S.K., 2008. An elastomeric conducting composite based on polyaniline coated nylon fiber and chloroprene rubber. Eur Polym J 44, 2418-2429.

Das, A., Costa, F.R., Wagenknecht, U., Heinrich, G., 2008. Nanocomposites based on chloroprene rubber: Effect of chemical nature and organic modification of nanoclay on the vulcanizate properties. Eur Polym J 44, 3456-3465.

Finlay, K., Gawryla, M.D., Schiraldi, D.A., 2008. Biologically based fiber-reinforced/clay aerogel composites. Ind Eng Chem Res 47, 615-619.

Fornes. T.D., Paul, D.R., 2003. Modeling properties of nylon 6/clay nanocomposites using composite theories. Polymer 44, 4993-5013.

Gatos, K.G., Sawanis, N.S., Apostolov, A.A., Thomann, R., Karger-Kocsis, J., 2004. Nanocomposite formation in hydrogenated nitrile rubber (HNBR)/organo-montmorillonite as a function of the intercalant type. Macromol Mater Eng 289, 1079-1086.

Gatos, K.G., Karger-Kocsis, J., 2007. Effect of the aspect ratio of silicate platelets on the mechanical and barrier properties of hydrogenated acrylonitrile butadiene rubber (HNBR)/layered silicate nanocomposites. Eur Polym J 43, 1097-1104.Gawryla, M.D., Nezamzadeh, M., Schiraldi, D.A., 2008. Foam-like materials produced from abundant natural resources. Green Chem 10, 1078-1081.

Gawryla, M.D., van der Berg, O., Weder, C., Schiraldi, D.A., 2009a. Clay aerogel/cellulose whisker nanocomposites: A nanoscale wattle and daub. J Mater Chem 19, 2118-2124.

Gawryla, M.D., Schiraldi, D.A., 2009b. Novel absorbent materials created via ice templating. Macromol Mater Eng 294, 570-574.

Guo, B.C., Chen, F., Lei, Y.D., Liu, X.L., Wan, J.J., Jia, D.M., 2009. Styrene-butadiene rubber/halloysite nanotubes nanocomposites modified by sorbic acid. Appl Surf Sci 255, 7329-7336.

Guth, E., 1945. Theory of filler reinforcement. J Appl Phys 16, 20-25.

Halpin, J.C., 1969. Stiffness and expansion estimates for oriented short fiber composites. J Compos Mater 3, 732-734.

Halpin, J.C., Kardos, J.L., 1976. Halpin–Tsai equations: a review. Polym Eng Sci 16, 344-352.

Johnson III, J.R., Spikowski, J., Schiraldi, D.A., 2009. Mineralization of clay/polymer aerogels: A bioinspired approach to composite reinforcement. Applied Materials & Interfaces 1, 1305-1309.

Kader, M.A., Nah, C., 2004. Influence of clay on the vulcanization kinetics of fluoroelastomer nanocomposites. Polymer 45, 2237-2247.

Kader, M.A., Kim, K., Lee, Y.S., Nah, C., 2006. Preparation and properties of nitrile rubber/montmorillonite nanocomposites via latex blending. J Mater Sci 41, 7341-7352.

Kim, J.Y., Kim, D.K., Kim, S.H., 2009. Effect of modified carbon nanotube on physical properties of thermotropic liquid crystal polyester nanocomposites. Eur Polym J 45, 316-324.

Leblanc, J.L., 2002. Rubber–filler interactions and rheological properties in filled compounds. Prog Polym Sci 27, 627-687.

Lee, S.H., Kim, S.Y., Youn, J.R., 2009. Effects of maleination and heat treatment on morphology and dynamic mechanical thermal behavior of polypropylene/organoclay nanocomposites. Composites: Part A 40, 968-974.

Li, P., Siddaramaiah, Kim, N.H., Heo, S.B., Lee, J.H., 2008. Novel PAAm/laponite clay nanocomposite hydrogels with improved cationic dye adsorption behavior. Composites: Part B 39, 756-763.

López-Manchado, M.A., Herrero, B., Arroyo, M., 2003. Preparation and characterization of organoclay nanocomposites based on natural rubber. Polym Int 52, 1070-1077.

Manitiu, M., Horsch, S., Gulari, E., Kannan, R.M., 2009. Role of polymer–clay interactions and nano-clay dispersion on the viscoelastic response of supercritical CO_2 dispersed polyvinylmethylether (PVME)–clay nanocomposites. Polymer 50, 3786-3796.

Pojanavaraphan, T., Magaraphan, R., 2008. Prevulcanized natural rubber latex/clay aerogel nanocomposites. Eur Polym J 44, 1968-1977.

Pojanavaraphan, T., Magaraphan, R., 2010. Fabrication and characterization of new semiconducting nanomaterials composed of natural layered silicates (Na^+-MMT), natural rubber (NR), and polypyrrole (PPy). Polymer 51, 1111-1123.

Praveen, S., Chattopadhyay, P.K., Albert, P., Dalvi, V.G., Chakraborty, B.C., Chattopadhyay, S., 2009. Synergistic effect of carbon black and nanoclay fillers in styrene butadiene rubber matrix: Development of dual structure. Composites: Part A 40, 309-316.

Raka, L., Gaceva, G.B., Lu, K., Loos, J., 2009. Characterization of latex-based isotactic polypropylene/clay nanocomposites. Polymer 50, 3739-3746.

Samakande, A., Sanderson, R.D., Hartmann, P.C., 2009. Rheological properties of RAFT-mediated poly (styrene-*co*-butyl acrylate)–clay nanocomposites

[P(S-*co*-BA)-PCNs]: Emphasis on the effect of structural parameters on thermo-mechanical and melt flow behaviors. Polymer 50, 42-49.

Somlai, L.S., Bandi, S.A., Schiraldi, D.A., 2006. Facile processing of clays into organically-modified aerogels. AIChE J 52, 1-7.

Stephen, R., Varghese, S., Joseph, K., Oommen, Z., Thomas, S., 2006. Diffusion and transport through nanocomposites of natural rubber (NR), carboxylated styrene butadiene rubber (XSBR) and their blends. J Memb Sci 282, 162-170.

Teh, P.L., Mohd Ishak, Z.A., Hashim, A.S., Karger-Kocsis, J., Ishiaku, U.S., 2004. Effects of epoxidized natural rubber as a compatibilizer in melt compounded natural rubber–organoclay nanocomposites. Eur Polym J 40, 2513-2521.

Varghese, S., Karger-Kocsis, J., 2003. Natural rubber-based nanocomposites by latex compounding with layered silicates. Polymer 44, 4921-4927.Wagener, R., Reisinger, T.J.G., 2003. A rheological method to compare the degree of exfoliation of nanocomposites. Polymer 44, 7513-7518.

Wouterson, E.M., Boey, F.Y.C., Hu, X., Wong, S.C., 2005. Specific properties and fracture toughness of syntactic foam: Effect of foam microstructures. Compos Sci Technol 65, 1840-1850.

Wu, Y.P., Jia, Q.X., Yu, D.S., Zhang, L.Q., 2004. Modeling Young's modulus of rubber–clay nanocomposites using composite theories. Polym Test 23, 903-909.

Yoo, Y., Paul, D.R., 2008. Effect of organoclay structure on morphology and properties of nanocomposites based on an amorphous polyamide. Polymer 49, 3795-3804.

Table 5.1 Formulation of compounding ingredients

Ingredients	Dry (parts by weight)
30 % Centrifuged rubber latex	100.0
10 % Potassium hydroxide solution	0.5
50 % Zinc oxide dispersion	1.0
50 % Calcium carbonate dispersion	10.0
50 % Sulfur dispersion (curative used)	1.0
50 % ZDEC dispersion (accelerator used)	0.75
50 % Wingstay-L dispersion (antioxidant used)	1.0
2 % Na^{+}-MMT dispersion	0, 1, 3, 5, 7

ZDEC, Zinc diethyl dithiocarbamate.

Table 5.2 Vulcanization characteristics, kinetic parameters, and activation energies of PNR and the corresponding composites obtained from ODR data

Samples	T_c (°C)	t_{90} (min)	D_{max} (dNm)	K	E_a (kJmol^{-1})
PNR	150	1.14	2.48	2.13	46.91
	160	0.77	2.98	2.95	
	170	0.53	2.87	3.10	
	180	0.50	2.97	5.61	
PNR/M1	150	1.42	2.26	1.93	55.25
	160	1.15	2.22	3.63	
	170	0.73	2.31	4.96	
	180	0.75	2.32	5.47	
PNR/M3	150	1.14	4.61	2.35	58.45
	160	0.82	4.48	3.14	
	170	0.73	4.67	5.63	
	180	0.51	3.60	6.57	
PNR/M5	150	1.05	6.60	1.96	63.34
	160	0.76	4.85	4.55	
	170	0.51	5.12	5.67	
	180	0.50	5.30	6.80	
PNR/M7	150	1.08	6.16	2.50	76.83
	160	0.76	6.21	5.50	
	170	0.51	6.53	8.20	
	180	0.51	5.79	10.81	

T_c—cure temperature; t_{90}—cure time; D_{max}—maximum rheometric torque; K—specific rate constant at temperature T; E_a—activation energy.

Table 5.3 Crosslink density (V_e), equilibrium toluene uptake, and thermodynamic parameters of PNR and the corresponding composites

Samples	V_e [a] ($molcm^{-3}$)	Equilibrium swelling ratio	ΔG ($Jmol^{-1}$)	ΔS ($Jmol^{-1}K^{-1}$)
PNR	5.18×10^{-5}	11.96	-6.02	2.02×10^{-2}
PNR/M1	3.88×10^{-5}	13.58	-4.36	1.46×10^{-2}
PNR/M3	3.35×10^{-5}	14.44	-3.70	1.24×10^{-2}
PNR/M5	2.77×10^{-5}	15.14	-2.99	1.00×10^{-2}
PNR/M7	2.64×10^{-5}	16.04	-2.83	0.95×10^{-2}

[a] Crosslink density [Pojanavaraphan and Magaraphan, 2008]: $V_e = -\left[\ln(1-\phi_r) + \phi_r + \chi\phi_r^2\right] / \left[V_1\left(\phi_r^{1/3} - \phi_r/2\right)\right]$, where V_e is the network chain density, χ is the Flory–Huggins polymer–solvent interaction (0.391), V_1 is the molar volume of toluene (106.3 cm^3mol^{-1}), and φ_r is the volume fraction of rubber in the swollen sample.

Table 5.4 Diffusion coefficient and transport properties of PNR and the corresponding composites

Samples	$D \times 10^4$ (cm^2s^{-1})	n	$k \times 10^2$ ($gg^{-1}s^{-n}$)
PNR	6.25	0.56	2.90
PNR/M1	21.15	0.56	7.85
PNR/M3	83.90	0.25	40.49
PNR/M5	209.30	0.03	75.23
PNR/M7	264.71	0.01	84.41

Table 5.5 Compression, density, and void volume fraction measurements of the studied materials

Samples	Initial modulus (kPa)	Reinforcing efficiency [b] (%)	Measured density (gcm^{-3})	Void [c] (%)
PNR [a]	17.3 ± 6.3	-	0.49 ± 0.03	48.6 ± 2.9
PNR/M1	19.3 ± 7.1	14.6	0.47 ± 0.01	50.7 ± 0.9
PNR/M3	23.0 ± 4.5	29.1	0.47 ± 0.02	51.4 ± 1.5
PNR/M5	22.5 ± 4.0	22.7	0.36 ± 0.03	63.1 ± 2.6
PNR/M7	35.4 ± 11.8	80.7	0.55 ± 0.05	43.5 ± 4.8

[a] The sample was produced from an aqueous dispersion containing 45 wt% solid NR.

[b] Reinforcing efficiency: $\% = [(M_c - M_m)/M_m] \times 100$, where M_m and M_c represent the modulus of the neat PNR and composites, respectively.

[c] Void volume fraction [Wouterson et al., 2005]: $V_v = 100 \times [(\rho_{theoretical} - \rho_{measured})/\rho_{theoretical}]$, where V_v is the void content, $\rho_{theoretical}$ is the theoretical density, calculated according to the rule of mixtures, and $\rho_{measured}$ is the measured density.

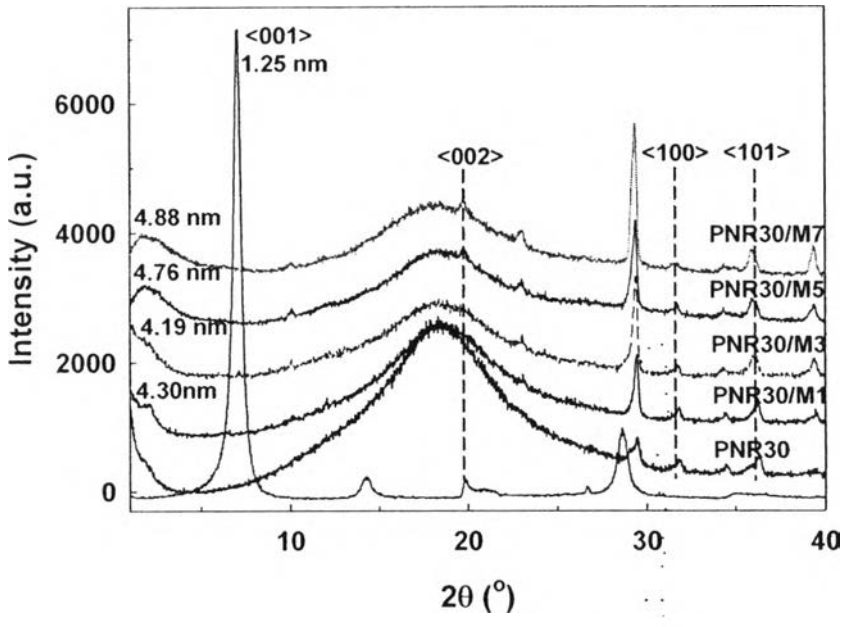

Figure 5.1 XRD patterns of the Na^{+}-MMT and the corresponding composites.

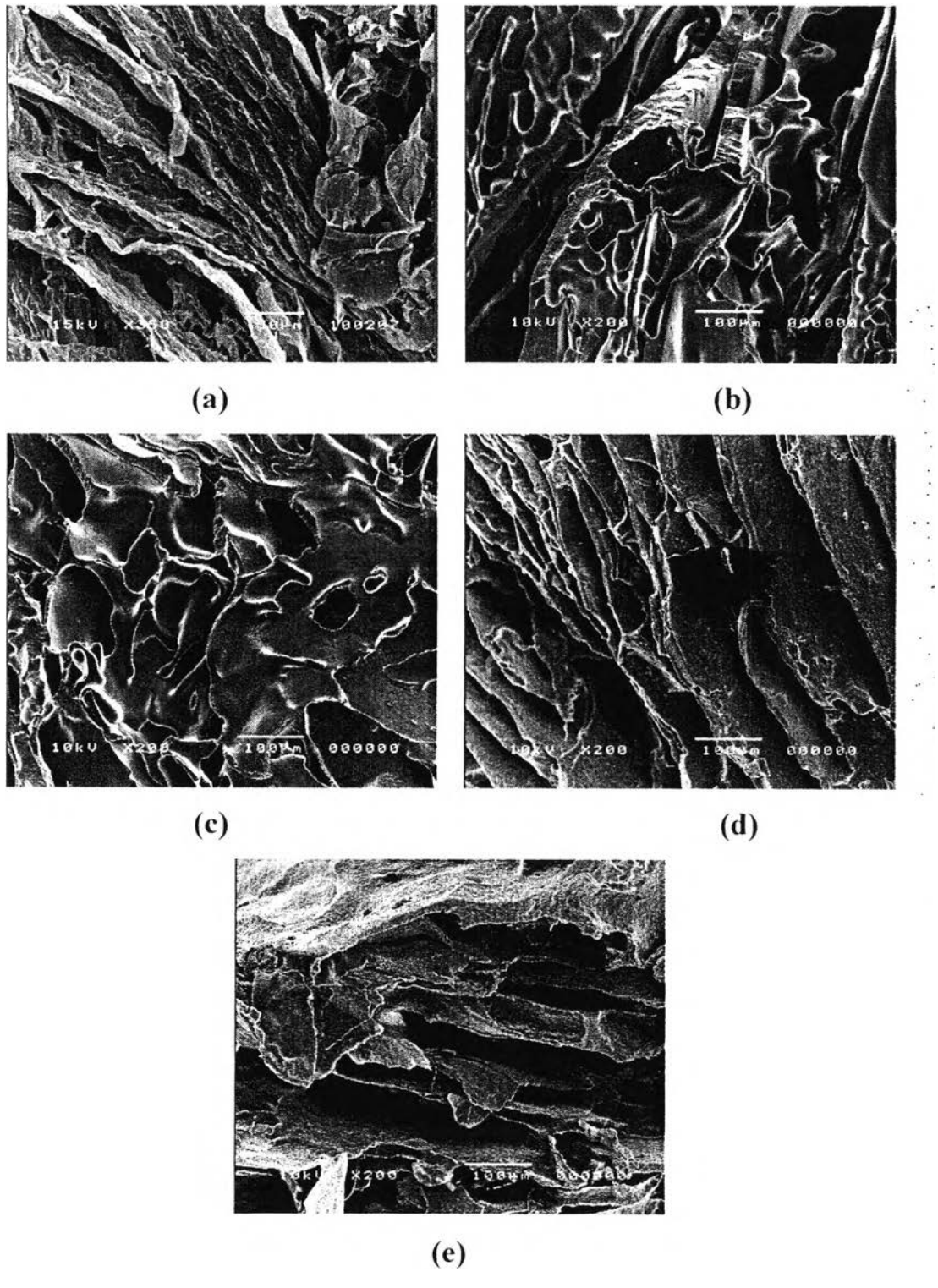

Figure 5.2 SEM micrographs of (a) Na^{+}-MMT aerogel, (b) PNR, (c) PNR/M1 composite, (d) PNR/M5 composite, and (e) PNR/M7 composite.

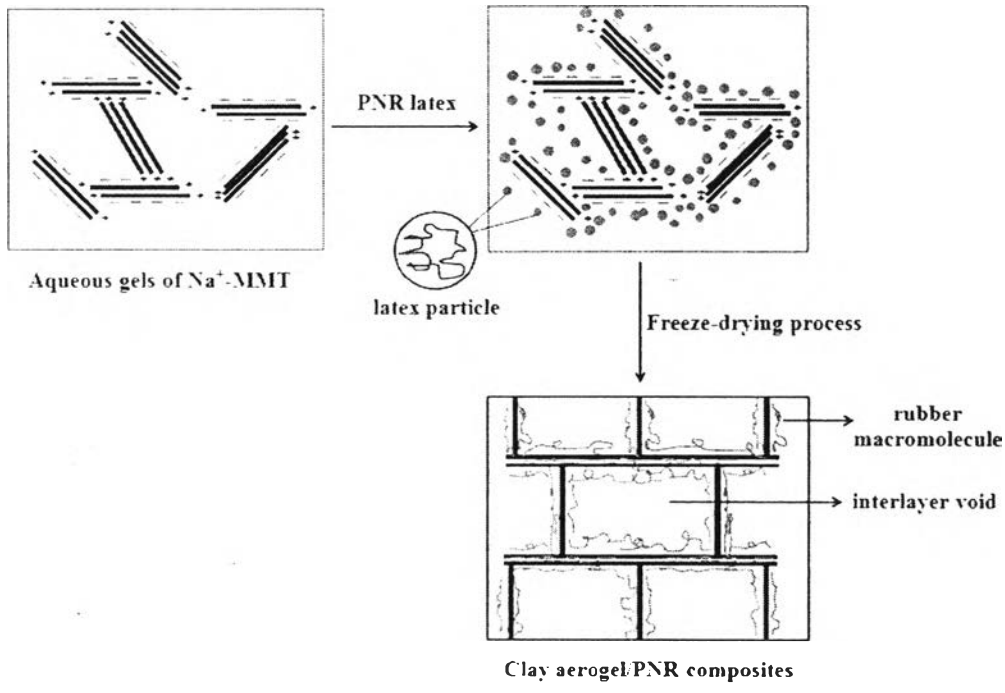

Figure 5.3 Schematic representation of the structure of Na^+-MMT aerogel/PNR composites.

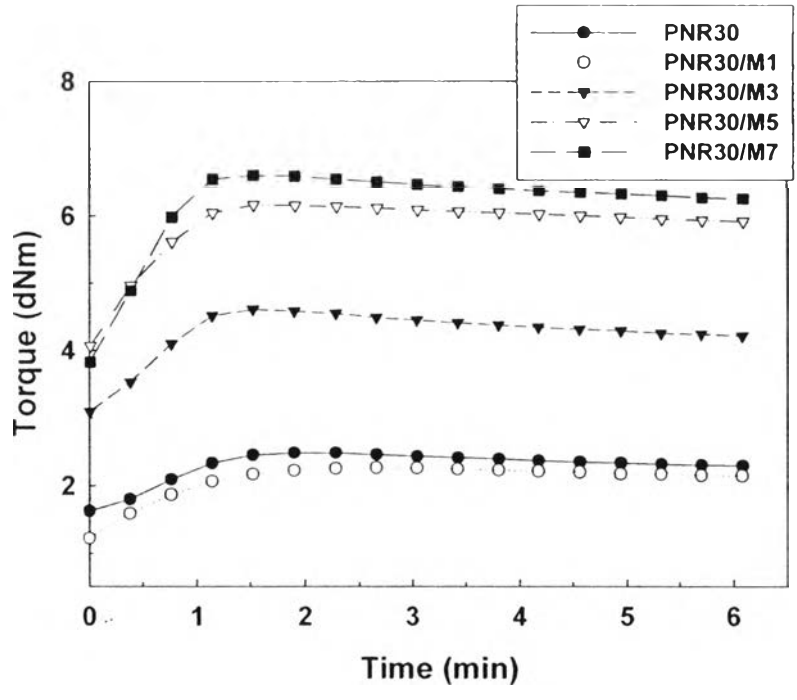

Figure 5.4 Rheographic curves of the neat PNR and the corresponding composites at 150°C.

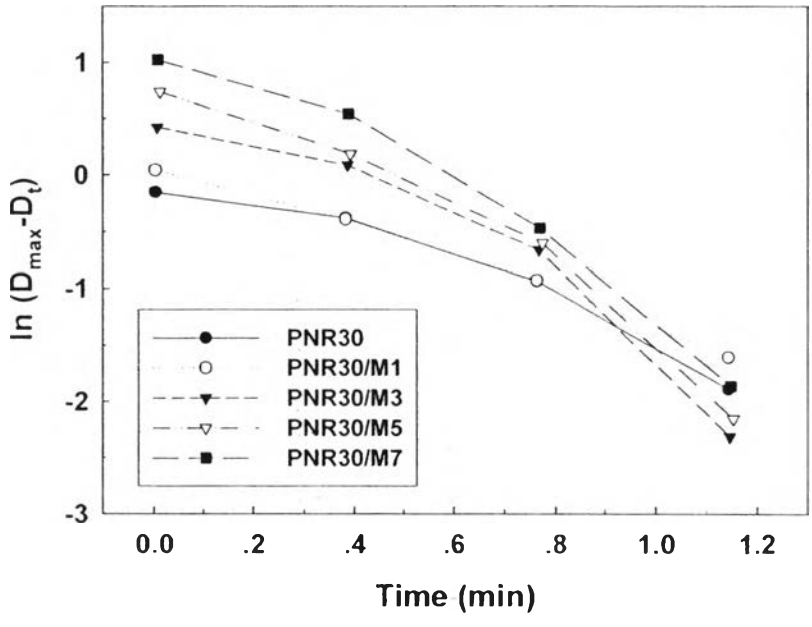

(a)

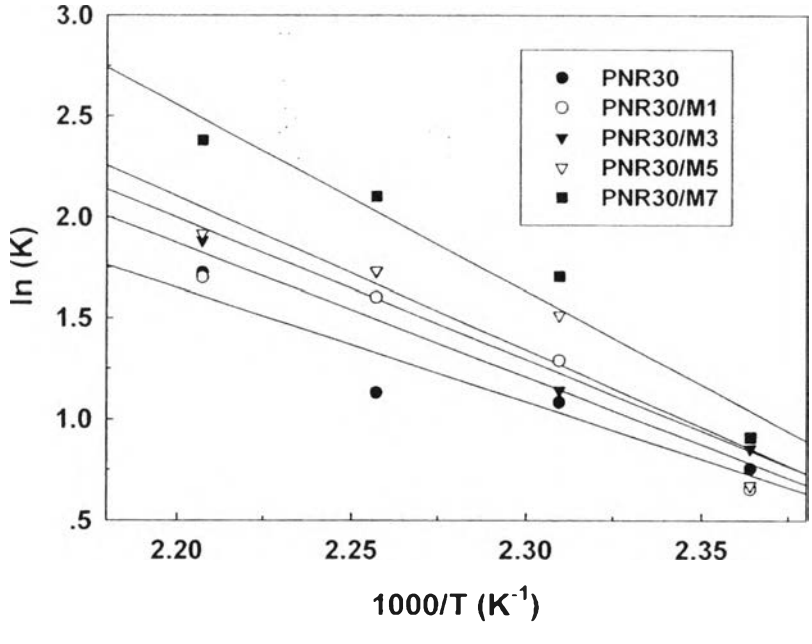

(b)

Figure 5.5 (a) Plot of ln (D_{max}-D_t) versus time and (b) Arrhenius plot between ln K versus 1000/T for the neat PNR and the corresponding composites.

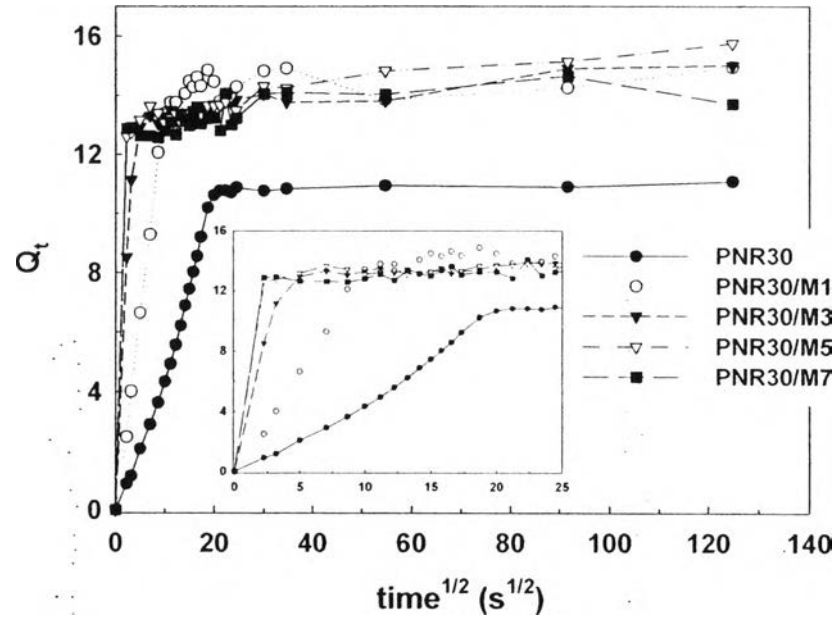

(a)

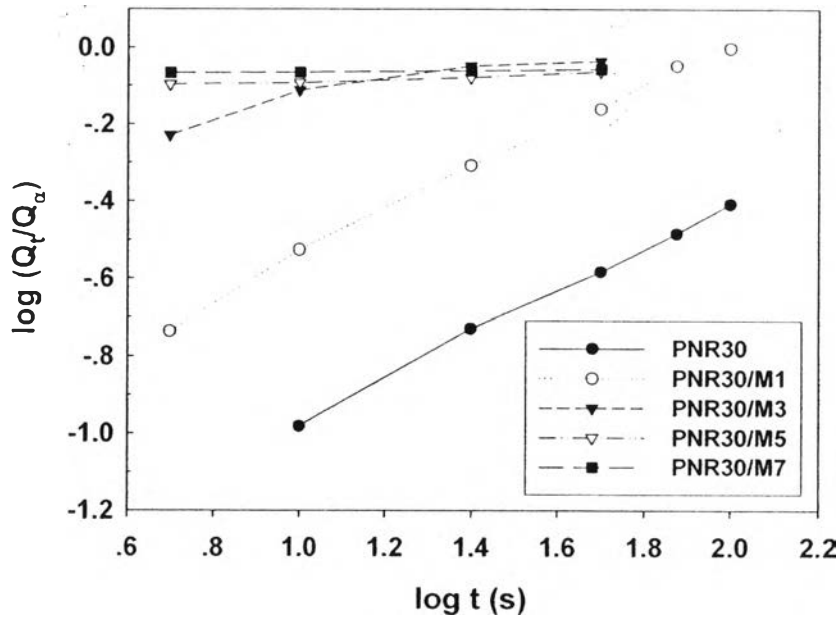

(b)

Figure 5.6 Plots of (a) Q_t against $t^{1/2}$ and (b) log (Q_t/Q_∞) against log t for the neat PNR and the corresponding composites in toluene at room temperature.

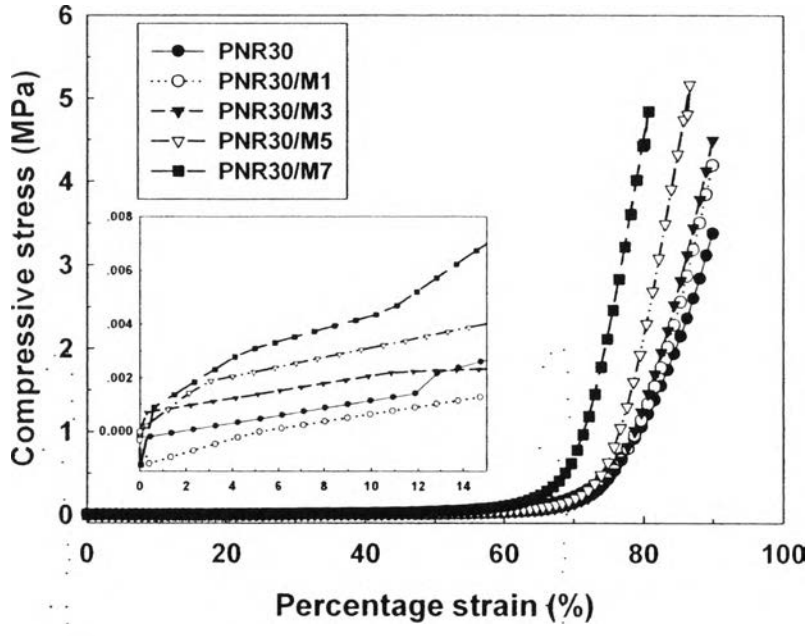

Figure 5.7 Stress–strain curves of the neat PNR and the corresponding composites.

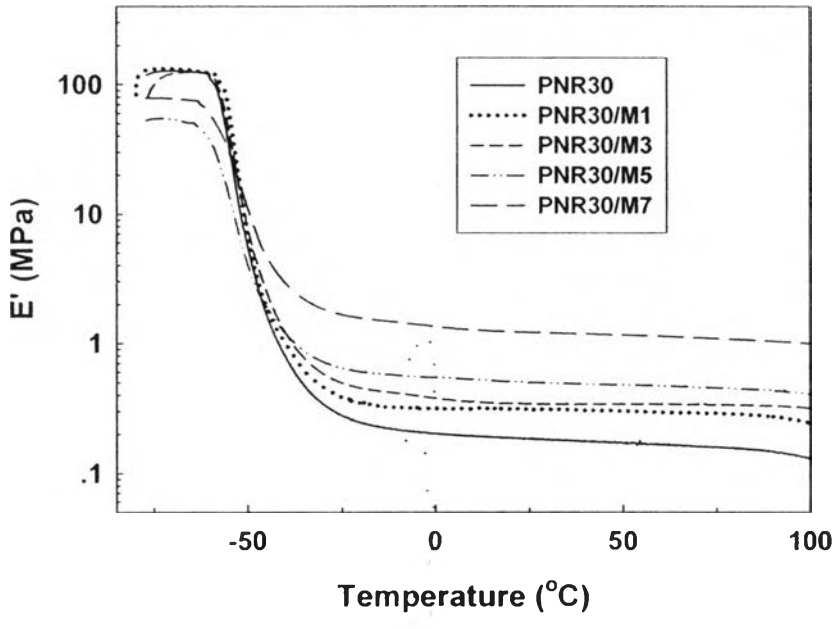

(a)

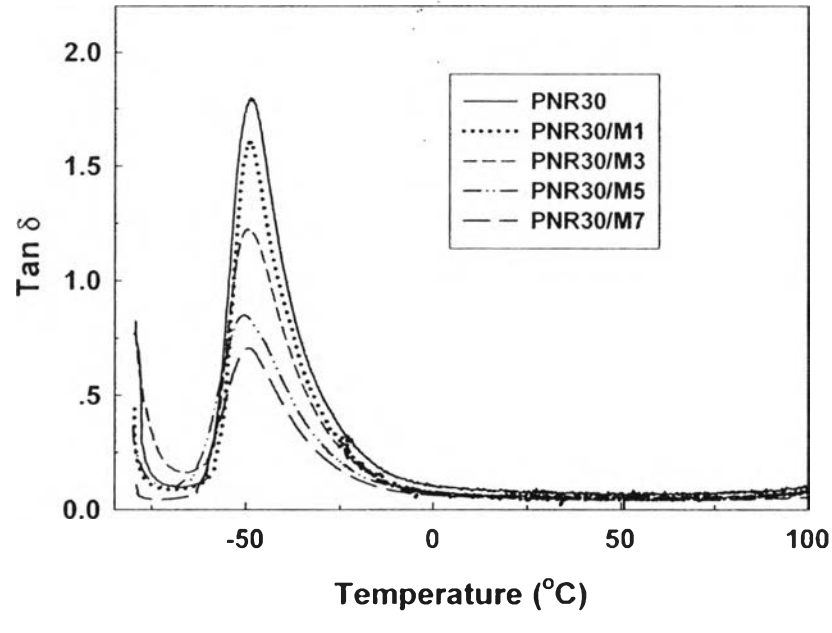

(b)

Figure 5.8 Temperature dependence of (a) storage modulus, E', and (b) loss tangent, tan δ, for the neat PNR and the corresponding composites.

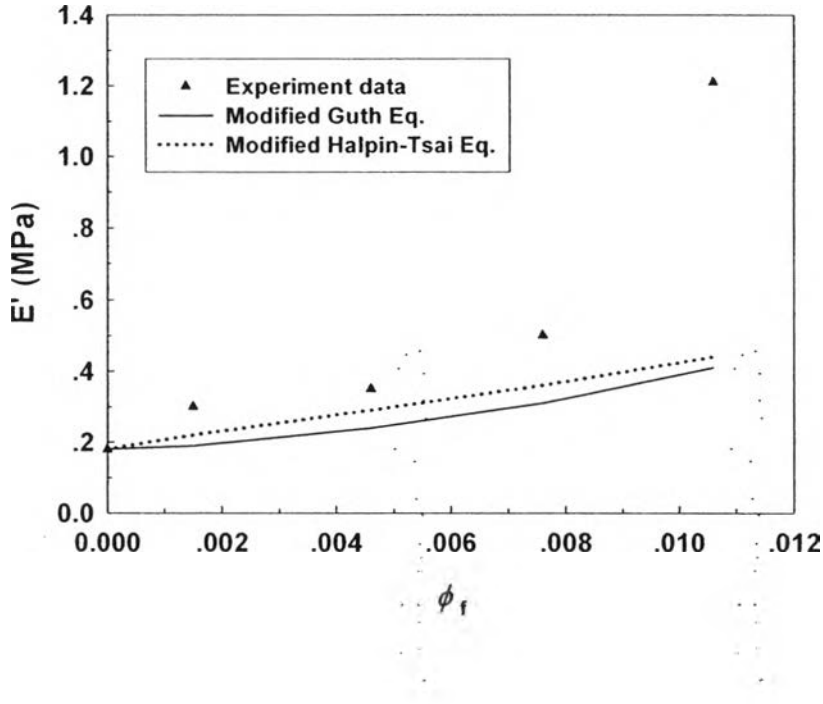

Figure 5.9 Comparison amongst experimentally measured dynamic modulus at room temperature and theoretical predictions by introducing MRF.

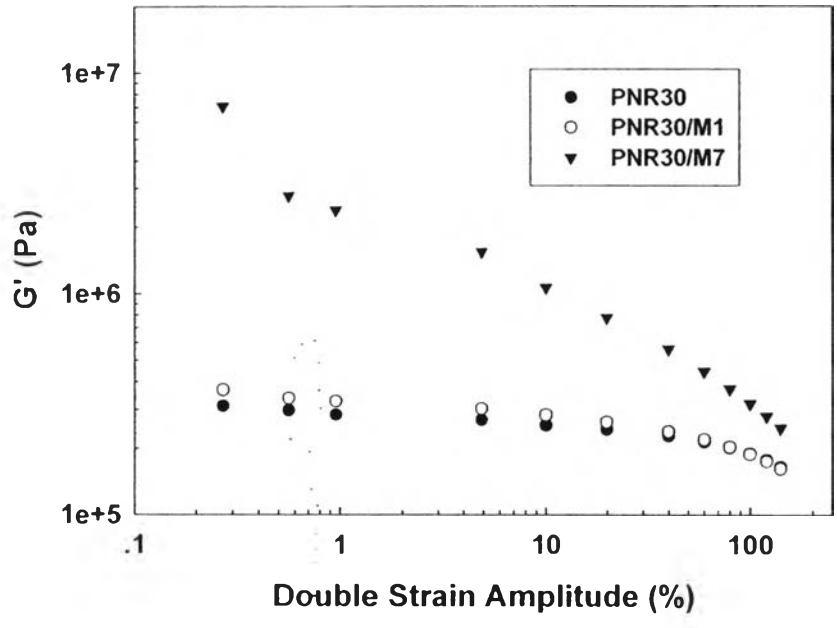

Figure 5.10 Strain sweep measurements of the neat PNR and the corresponding composites at 150°C.

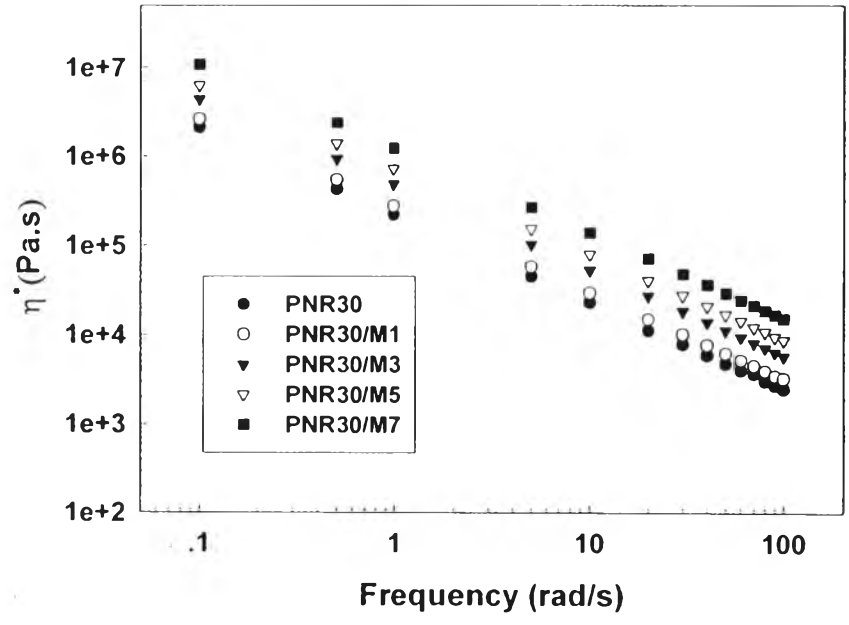

(a)

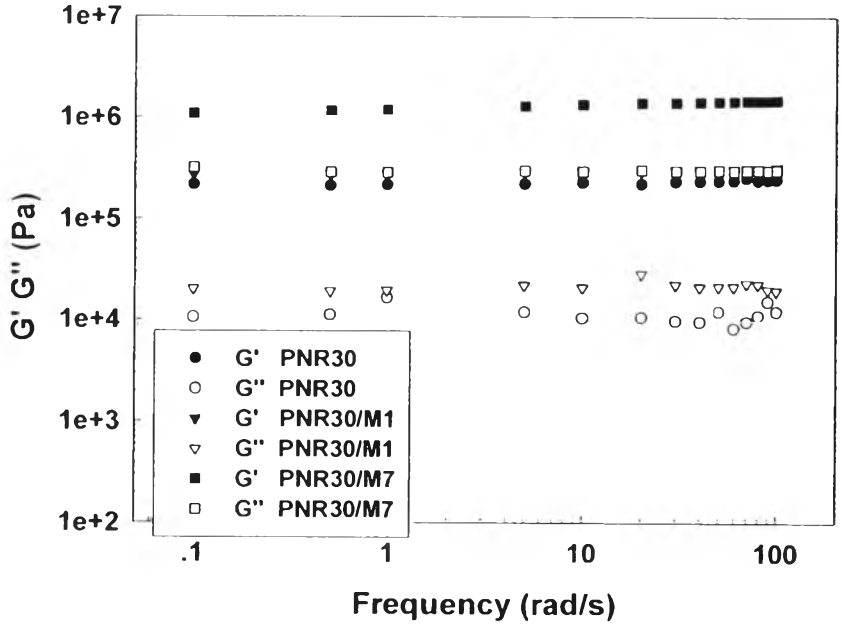

(b)

Figure 5.11 Frequency dependence of (a) dynamic complex viscosity, η^*, and (b) dynamic storage modulus, G', and loss modulus, G'', of the neat PNR and the corresponding composites at 150°C.